# Effects of Precipitation on Propagation at 0.63, 3.5, and 10.6 Microns

By T. S. CHU and D. C. HOGG

*The attenuation and scattering of laser beams by rain, fog, and snow have been calculated and measured at 0.63, 3.5, and 10.6μ. Attenuation of the infrared wavelengths by light fog is up to one order of magnitude less than at 0.63μ. But for dense fog, calculation shows that the attenuation at 10.6μ can exceed 40 dB per km. It is found that attenuation by rain can be calculated to good accuracy from average path rain rates provided that forward scattering is taken into account; this scattering reduces the attenuation.*

*Measurements of propagation through precipitation over a 2.6 km path are discussed in detail and are found to be consistent with predictions. The wavelength dependence of attenuation is found to vary from one fog to another because of different drop-size distributions. Attenuation of 0.63μ in rain showers is about 20 per cent less than at 3.5μ and is, of course, much less than the attenuation in fog. But even for extremely heavy rain showers, the 0.63μ attenuation never exceeded 20 dB per km, which is less than the attenuation of millimeter waves under such conditions. Both the attenuation and foreward scattering properties of snow appear to be between those of fog and rain.*

## I. INTRODUCTION

It is well known that optical waves suffer much attenuation in propagation through precipitation in the atmosphere. Penetration of light through a dense fog is much more difficult than through a heavy shower. One would also expect similar phenomena for near infrared waves. However, quantitative data are necessary in order to evaluate the potential use of lasers for short range communication through the atmosphere. Attenuation by precipitation is the dominant factor in determining the feasibility of open-air laser communication systems. The interesting fluctuations of laser beams caused by turbulence in the clear atmosphere are not discussed here.

The gas lasers which provide significant amounts of power within the infrared windows of the clear atmosphere are $3.5\mu$ and $10.6\mu$; $3.39\mu$ is not suitable because it is attenuated by the small amount of methane in the air.[1] The wavelengths of visible gas lasers with suitable output power are $0.49\mu$ and $0.63\mu$. Since the attenuation of optical waves in a fog is largely the result of scattering by numerous small drops, it is not likely that transmission of $0.49\mu$ and $0.63\mu$ through a fog would differ appreciably. The literature reveals that the attenuation of blue light ($\sim 0.49\mu$) through a light fog is somewhat greater than that of red light ($\sim 0.63\mu$), while their attenuations in a dense fog differ little from one another.[2] In this study, $0.63\mu$ is the visible wavelength used.

Some computed results of attenuation by precipitation at the wavelengths of $0.63\mu$, $3.5\mu$, and $10.6\mu$ are given first. The effect of forward scattering is examined using a Gaussian model for the scattering pattern of a rain drop and a single scattering model is used to describe the broadening of a laser beam by precipitation. Then the results of measurements of attenuation by precipitation over a 2.6 km path at these three wavelengths are described. Some of the measured data have been discussed briefly in previous notes.[3, 4]

The measured attenuation by rain is compared with that calculated from the rainfall measured on the path. Optical attenuation by fog is compared with total liquid water content derived from path-loss measurements taken on a radar operating at a wavelength of 3 mm. Similar quantitative correlations have not been made for attenuation by snow because of the lack of an independent physical measurement for this form of precipitation.

## II. ATTENUATION CALCULATIONS

### 2.1 *Method of Computation*

The total power removed from a laser beam by a precipitation particle, say a spherical drop of radius $a$, is given by

$$E = SC(a, \lambda) \tag{1}$$

where $S$ is the magnitude of the incident Poynting vector, and $C(a, \lambda)$ is the total or extinction cross section of the drop. The change in $S$ upon passing through a layer of precipitation $\Delta z$ is

$$\Delta S = -S\,\Delta z \int_0^\infty n(a)C(a, \lambda)\,da \tag{2}$$

where $n(a)da$ is the number of drops per unit volume within the range $(a, a+da)$. Integrating equation (2) yields

$$S = S_0 e^{-\int \alpha dz} \tag{3}$$

where

$$\alpha = \int_0^\infty n(a)C(a, \lambda)\, da. \tag{4}$$

The total cross section is often normalized with respect to the geometrical cross section

$$Q(a, \lambda) = \frac{C(a, \lambda)}{\pi a^2}. \tag{5}$$

Since the energy removed is partly scattered and partly absorbed by the particle, the total cross section is divided into scattering and absorption cross sections:

$$Q_{ext} = Q_{scat} + Q_{abs}. \tag{6}$$

The $Q$'s are sometimes called efficiency factors. Notice that part of the energy represented by the scattering cross section is scattered forward; this leads to a decrease in attenuation as discussed in Section III.

The attention coefficient in equation (4) may be calculated if the particle-size distribution and the cross sections are given. Equation (4) gives the extinction, scattering, or absorption coefficients when the appropriate cross section is substituted.* We take the shape of the water drops in fog and rain to be spherical. With this assumption, it is not a prohibitive task to use Mie's rigorous expressions to calculate the extinction and absorption cross sections of the drops. However, very simple approximate formulas are quite applicable here in view of the uncertain drop-size distributions and the doubtful sphericity. Using a combination of geometrical optics and Huygen's principle, Van de Hulst[5] obtained the following formulas for the extinction and absorption cross section:

$$Q_{ext} = 2 - 4e^{-\rho \tan \beta}\left(\frac{\cos \beta}{\rho}\right) \sin (\rho - \beta) - 4e^{-\rho \tan \beta}\left(\frac{\cos \beta}{\rho}\right)^2 \cos (\rho - 2\beta) + 4\left(\frac{\cos \beta}{\rho}\right)^2 \cos 2\beta \tag{7a}$$

* Extinction is often used in optical terminology for attenuation; however, it is misleading. It is more exact to designate the extinction coefficient as the attenuation coefficient without forward scattering corrections.

$$Q_{abs} = 1 + \frac{e^{-4xn'}}{2xn'} + \frac{e^{-4xn'} - 1}{8x^2n'^2} \tag{7b}$$

where

$$\rho = \frac{4\pi a}{\lambda}(n - 1), \qquad \tan \beta = \frac{n'}{n - 1}, \qquad x = \frac{2\pi a}{\lambda},$$

and $n$ and $n'$ are the real and imaginary parts of the refractive index, respectively. The above two expressions are derived under the assumptions $(n - 1) \ll 1$, $n' \ll 1$, $2\pi a/\lambda \gg 1$. Numerical comparison indicates[5] that the essential features of the cross section curves using equation (7) remain correct for $| n - 1 - in' | \lesssim 1$ and $2\pi a/\lambda \gtrsim 1$. When $\rho \ll 1$, equation (7) reduces to

$$Q_{ext} = \tfrac{4}{3}\rho \tan \beta + \tfrac{1}{2}\rho^2(1 - \tan^2 \beta) \tag{8a}$$

$$Q_{abs} = \tfrac{4}{3}\rho \tan \beta - \rho^2 \tan^2 \beta. \tag{8b}$$

### 2.2 *Refractive Indices*

Figure 1 shows the complex refractive index $(n - in')$ of liquid water in the visible and near infrared region. For the wavelengths below $18\mu$ the data have been taken from the tabulation by Centeno[6] except for those of $n'$ in the $2.8\mu$ band where Centeno's values are too low and have been replaced by the Bayly results.[7] No serious changes

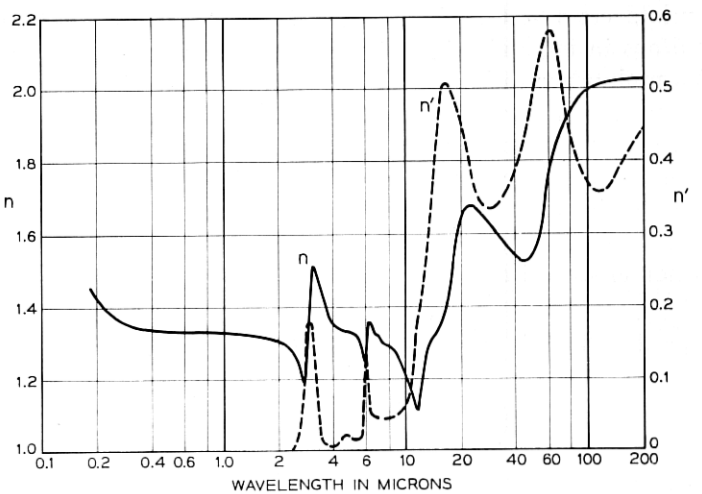


Fig. 1 — Complex refractive index $(n - in')$ of liquid water.

at other wavelengths are reported in more recent literature. In particular, for the three wavelengths we investigated, the complex refractive indices of liquid water are well agreed upon:

$$\lambda = 0.63\mu, \quad n = 1.33, \quad n' \sim 10^{-6}$$

$$\lambda = 3.5\mu, \quad n = 1.42, \quad n' = 0.013$$

$$\lambda = 10.6\mu, \quad n = 1.18, \quad n' = 0.08.$$

The curves beyond $18\mu$ in Figure 1 have been obtained from Kislovskii.[8] Most measurements of the refractive index of water have been conducted at 20°C, but it is known that as the temperature of the water is increased, the position of maximum absorption is shifted to slightly shorter wavelengths.[9, 10] However, detailed information on temperature dependence seems to be lacking. Much less data have been published for the complex refractive index of ice than for water. Figure 2, ice at −10°C, is reproduced from Kislovskii for the sake of completeness.

### 2.3 *Cross Sections and Attenuation Coefficients for Monodisperse Drop-Size Distribution*

Using equations (7) and the above values of the complex refractive indices, extinction and absorption cross sections have been computed as a function of radius of water spheres for the three wavelengths we mentioned. The data are shown in Figure 3. When the radius of the water sphere becomes large, say 1 mm (that is, about the size of

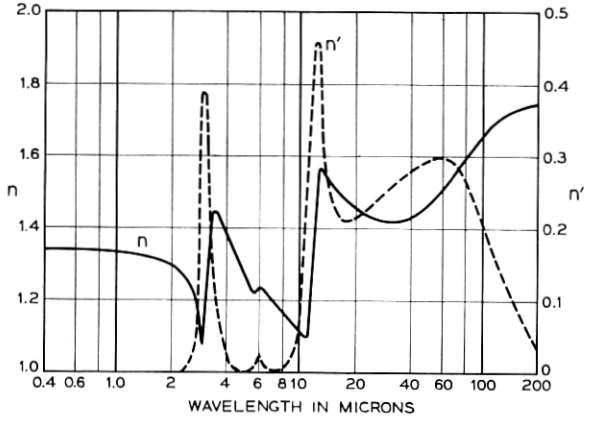


Fig. 2 — Complex refractive index ($n - in'$) of ice.

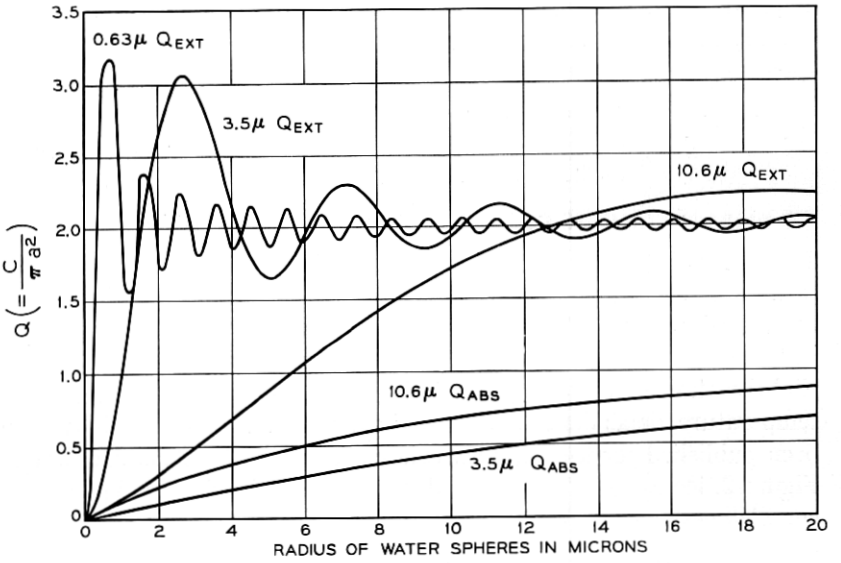


Fig. 3 — Approximate extinction and absorption cross sections.

a rain drop), the extinction cross sections approach two, while the absorptive cross sections at $3.5\mu$ and $10.6\mu$ approach unity. The absorption cross section of $0.63\mu$ does not appear in Figure 3 because pure water is practically lossless at visible wavelengths. The extinction cross section for $3.5\mu$ remains substantially less than that of $0.63\mu$ only when the radius of water sphere is smaller than $1\mu$; also, in that range, the extinction cross section of $10.6\mu$ almost entirely results from absorption. The longer wavelength and the lower refractive index push the first maximum of the $10.6\mu$ extinction cross section to an "$a$" of about $19\mu$.

Although fogs and rains never have drops of a single radius, it is instructive to calculate the attenuation coefficients for this ideal case. If we substitute

$$n(a) = \frac{w}{\frac{4}{3}\pi a^3}\,\delta(a) \tag{9}$$

into equation (4), where $w$ is the liquid water density and $\delta(a)$ is the Dirac delta function, then the extinction coefficient of liquid water becomes

$$\alpha = \frac{3}{4}\frac{Q_{ext}}{a}\frac{\text{nepers}}{\text{km}}\Big/\frac{\text{mg}}{\text{m}^3} = 3.25\,\frac{Q_{ext}}{a}\frac{\text{dB}}{\text{km}}\Big/\frac{\text{mg}}{\text{m}^3} \tag{10}$$

where the radius of water sphere "$a$" is in microns. The extinction and absorption coefficients obtained using equation (10) are plotted in Figure 4.

The vast difference in attenuation by rain and fog is very clear from equation (10). Although the liquid water content of a typical heavy shower, say 1000 mg/m$^3$, is ten times that of a typical dense fog, say 100 mg/m$^3$, the fog drop radius is about one thousandth that of a rain drop. This is the primary reason why attenuation by rain is two orders of magnitude less than that of fog at optical wavelengths. For rains with drop radii about 1mm, the extinction coefficient is only 0.0065 (dB/km)/(mg/m$^3$) (see Figure 4), thus a fairly heavy shower with a liquid water content of 1 g/m$^3$ (rain rate about 25 mm per hour) has an extinction of about 6.5 dB/km for both optical and near-infrared wavelengths.

At least half of the attenuation resulting from rain at 3.5$\mu$ and

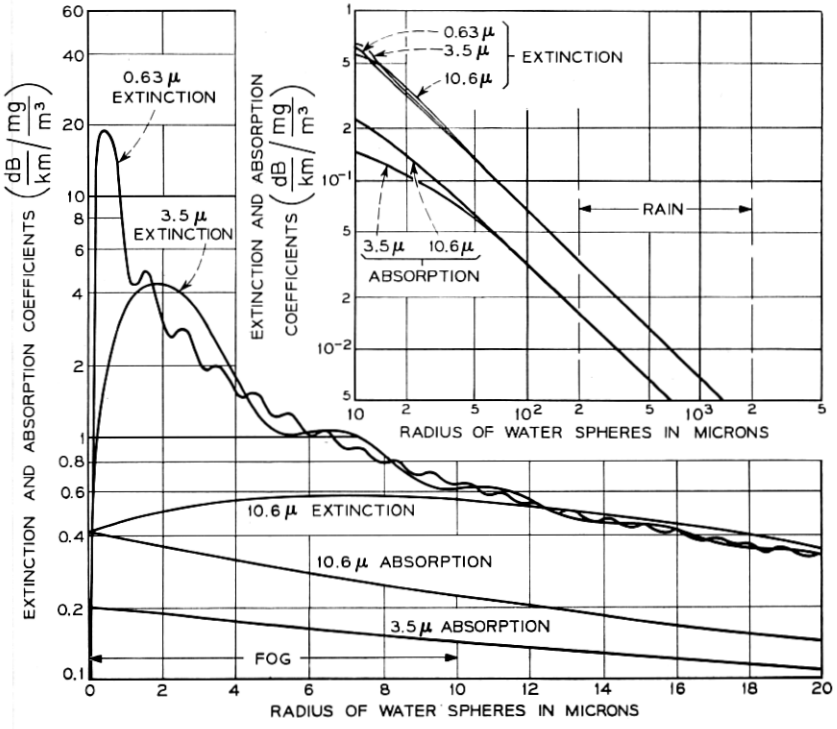


Fig. 4 — Extinction and absorption coefficients of precipitation with monodisperse drop-size distribution.

10.6$\mu$ is absorptive loss while at 0.63$\mu$ it is caused almost entirely by scattering, as seen from Figure 4.

Attenuation by fog is contributed largely by water drops less than a few microns in radius, therefore much of the 10.6$\mu$ attenuation is absorptive loss, as implied by equation (8) and Figure 4. The extinction coefficient of fog is expected to be substantially less (up to one order of magnitude) at 10.6$\mu$ than at 0.63$\mu$ where scattering predominates. However, heavy fogs with liquid water contents exceeding 0.1gm/m$^3$ will attenuate 10.6$\mu$ more than 40 dB/km.

Attenuation by fog at 3.5$\mu$, largely caused by scattering, remains significantly less than that of 0.63$\mu$ only if the fog drop radii are smaller than 1$\mu$, as is also true for haze. Fogs which consist of drops with an average radius of 5$\mu$ are expected to attenuate about the same amount at optical and shorter near-infrared wavelengths.

### 2.4 *Calculations for Realistic Drop Size Distributions*

Experimental difficulty and natural variations have caused gross inconsistency among the published data on measured fog drop-size distributions. Most of the measuring instruments fail to respond to droplets less than one micron in diameter, yet there are indications that the number density continues to increase as the diameter of fog drops decreases toward one micron. The relatively consistent information seems simply to be that the number density decreases for the larger drop radii.

For example, Eldridge's measurement shows that the number density decreases approximately with the inverse square of the drop diameter.[11] In searching for a realistic drop-size distribution for fog, the following model[12] for the number density, appeared to be plausible:

$$n\left(\frac{a}{a_m}\right) = A\left(\frac{a}{a_m}\right)^{\alpha} \exp\left[-B\left(\frac{a}{a_m}\right)^{\gamma}\right]. \tag{11}$$

Here

$$A = \left(\frac{\alpha}{\gamma}\right)^{(\alpha+1)/\gamma} \frac{\gamma}{\Gamma\left(\frac{\alpha+1}{\gamma}\right)} \frac{N}{a_m} \quad \text{and} \quad B = \frac{\alpha}{\gamma}.$$

$N$ is the number of drops per unit volume (say cm$^3$), $a_m$ the radius of the drops with the maximum number density, and $\alpha$ and $\gamma$, parameters which can be adjusted to fit an observed fog particle size distribution. The liquid water density appropriate to the above model

is easily obtained by integrating equation (11).

$$W = \int_0^\infty n\tfrac{4}{3}\pi a^3\, da = \frac{4\pi}{3}\left(\frac{\gamma}{\alpha}\right)^{3/\gamma} \frac{\Gamma\left(\frac{\alpha+4}{\gamma}\right)}{\Gamma\left(\frac{\alpha+1}{\gamma}\right)} a_m^3 N. \tag{12}$$

In Figure 5 four plots of equation (11) are given for several indicated combinations of parameters. Three of these exhibit a slope on the larger drop side of the maximum ($a > a_m$) similar to that of Eldridge's measured distribution. The other combination of parameters ($\alpha = 2$, $\gamma = 3$) shown in Figure 5 corresponds to the asymptotic distribution of coagulating particles[13] and has a sharp decreasing rate on both sides of the maximum number density.

Using these model distributions, extinction coefficients have been plotted versus the radius at maximum number density, $a_m$, in Figure 6. These curves merge at somewhat smaller values of $a_m$ than do the corresponding curves for constant drop radius in Figure 4 because

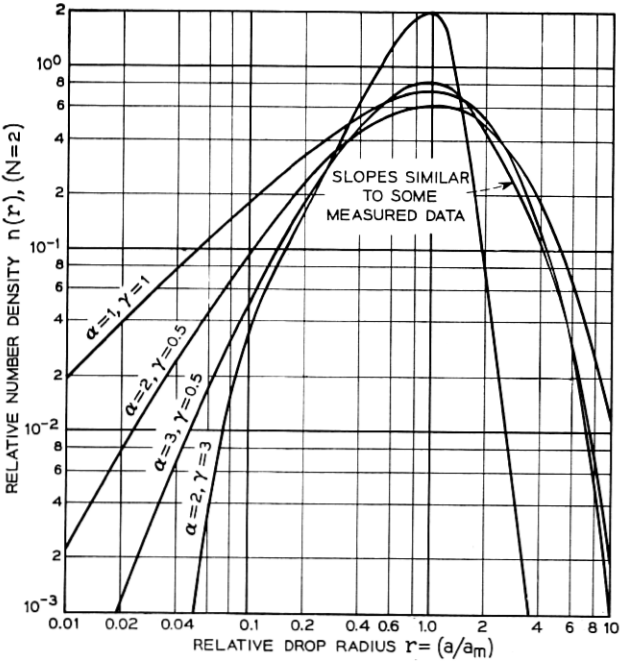


Fig. 5 — Drop size distribution of fog models. $n(r) = Ar^\alpha \exp[(-\alpha/\gamma)r^\gamma]$ $A = (N/a_m)\ (\alpha/\gamma)^{(\alpha+1)/\gamma}\ \gamma/\Gamma[\alpha+1)/\gamma]$, and $a_m$ = radius of drops with maximum number density.

the drops larger than $a_m$ contribute more to the extinction than do smaller ones.* The similarity between Figures 6(a) and 6(c) is attributed to the similar average slopes on the larger drop side of the corresponding distributions in Figure 5.

It is interesting to compare the above model with the Junge dis-

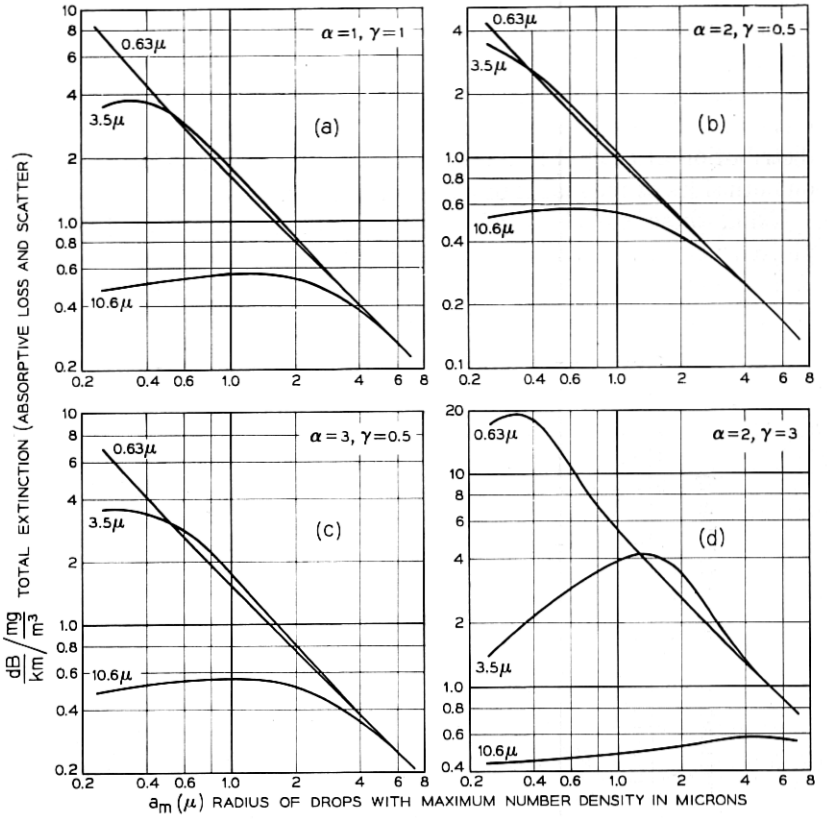


Fig. 6 — Extinction of coefficients for various fog models.

tribution[14] which states that $n(a) = ca^{-p}$ where $2 \leq p \leq 4$.[15, 16] This simple relation points out the importance of decreasing number density for the larger drops; however, more parameters, such as those offered in equation (11), are needed to describe both ends of the

* Although more extinction is obtained *for the same amount of liquid water* in the form of smaller drops than in the form of larger drops, the extinction cross section of a larger drop is, of course, greater than that of a smaller drop.

distribution. Since the extinction cross section is of the order of the geometrical cross section $\pi a^2$, the decreasing rate of larger drops can be approximated by the inverse square power ($p \sim 2$) only in a limited range beyond which the number density must decrease much more rapidly to insure convergence of the integral in equation (4).

Raindrop size distributions measured at ground level seem to be fairly consistent among the published data. The Laws and Parsons[17] distributions which have been virtually confirmed by later workers are illustrated in Figure 7 and are readily available in tabulations.[18] Substituting these well-known distributions into equation (4) yields the extinction coefficient versus rain rate shown as the upper solid curve in Figure 8. Notice that the total extinction is the same for the visible and near-infrared wavelengths. Half of the extinction coefficient at $3.5\mu$ or $10.6\mu$ is contributed by the absorptive loss as illustrated in Figure 8.

## III. FORWARD SCATTERING

The energy intercepted by precipitation particles is partially scattered forward, toward the receiver, and this reduces the attenuation. Here is an approximate calculation for predicting the reduction of

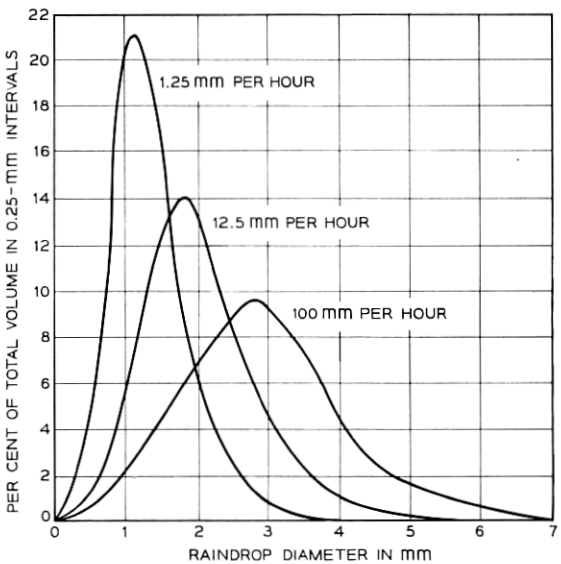


Fig. 7 — Raindrop size distributions by Laws and Parsons.

attenuation at $0.63\mu$ and $3.5\mu$ by forward scattering during rain, and a single-scattering model for beam broadening.

### 3.1 *Approximate Correction Factor for Attenuation by Rain*

The forward scattering pattern of a rain drop is assumed to be a Gaussian beam with an effective aperture area equal to the geometrical cross section of the water sphere.[19] Using the geometrical parameters illustrated in Figure 9, the scattering pattern of a raindrop of radius $a$ situated at $(\rho, \varphi, Z)$ is taken to be

$$\frac{2}{\pi w_s^2} e^{-2R^2/w_s^2}$$

where

$$w_s^2 \cong w_{os}^2\left[1 + \left(\frac{\lambda(L - Z)}{\pi w_{os}^2}\right)^2\right]$$

and the effective aperture area is $2\pi w_{os}^2 = \pi a^2$. The beam from the transmitter, $T$, is taken to be

$$\frac{2}{\pi w^2} e^{-2\rho^2/w^2}$$

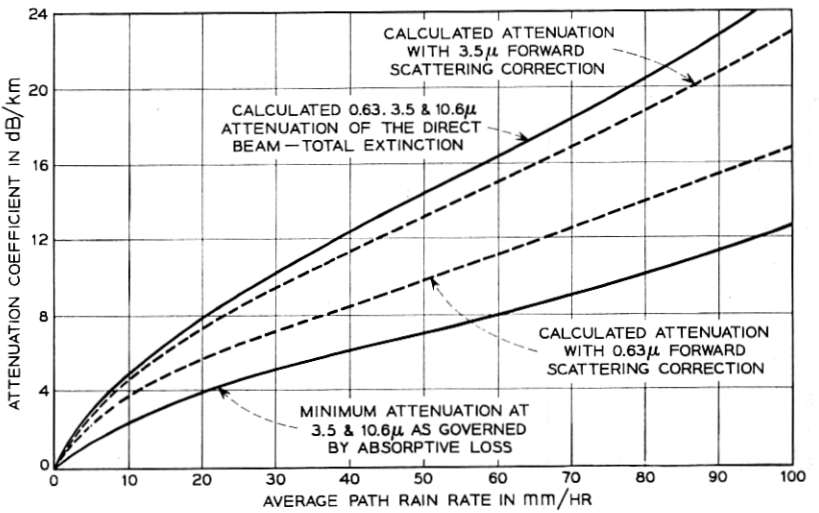


Fig. 8 — Rain attenuation coefficient for a 2.6 km path.

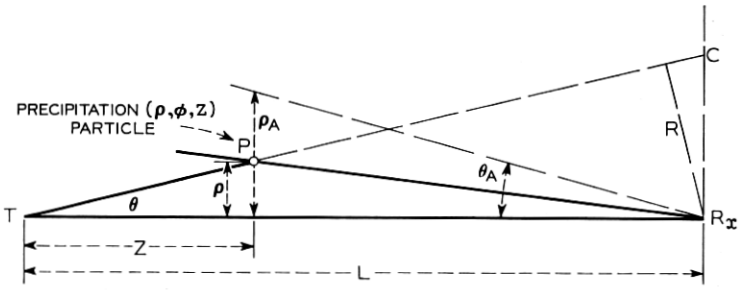


Fig. 9 — Geometry for forward scattering.

where

$$w^2 = w_{oT}^2\left[1 + \left(\frac{\lambda Z}{\pi w_{oT}^2}\right)^2\right]$$

and $w_{oT}$ is the minimum beam radius, located at the uniphase transmitting aperture. Then the attenuation in a path of length $L$ is:

$$\alpha L(1 - \bar{\beta}) = \int_0^L \alpha\, dZ\left[1 - \frac{Q_{sca}}{Q_{ext}}\frac{1}{\frac{2}{\pi w_T^2}}\right.$$

$$\left.\cdot \int_0^{\rho_A} \frac{2}{\pi w^2} e^{-2\rho^2/w^2} \frac{2}{\pi w_s^2} e^{-2R^2/w_s^2} 2\pi\rho\, d\rho\right]. \qquad (13)$$

$\alpha$ is the extinction coefficient (the attenuation coefficient without forward scattering correction), $\beta$ the reduction factor resulting from forward scattering, $Q_{sca}/Q_{ext}$ the fraction of the intercepted energy available for forward scattering, $2/\pi w_T^2$ the maximum flux of the unattenuated transmitted beam at the receiver

$$\left(w_T^2 = w_{oT}^2\left[1 + \left(\frac{\lambda L}{\pi w_{oT}^2}\right)^2\right]\right),$$

and $\rho_A/(L - Z) = \theta_A$ the acceptance angle of the receiver. It is easily shown from the geometry of Figure 9 that $R/\rho = L \cos\theta/Z$; thus when $\theta$ is small, as it is in practice, $R \cong \rho L/Z$. If the acceptance angle of the receiver is large compared with the scattering beamwidth of the rain drop, $\rho_A$ can be replaced by $\infty$.

The above approximations simplify evaluation of the inner integral in (13) and lead to the following expression for the forward scattering

correction factor:

$$\bar{\beta} = \frac{1}{L}\frac{Q_{scs}}{Q_{ext}}\int_0^L \frac{w_T^2}{w_s^2 + w^2\left(\frac{L}{Z}\right)^2}\,dZ. \tag{14}$$

Using equation (14), $\bar{\beta}$ versus raindrop radius has been computed for $L = 2.6$ km, $\lambda = 3.5\mu$, $w_{oT} = 0.55$ cm, and $\lambda = 0.63\mu$, $w_{oT} = 0.25$ cm. Table I gives the data. The two values of $w_{oT}$ are the clear weather beamwidths in our experiments. Upon numerical integration over the raindrop size distribution one obtains the dashed curves in Figure 8. The above approximate calculation is essentially a crude multiple scattering model for very narrow beams because equation (13) implies that the forward scattering energy effectively rejoins the original transmitting beam.

### 3.2 *A Single Scattering Model for Beam Broadening*

Measurements discussed later show that various degrees of beam broadening occur when a $0.63\mu$ laser beam propagates through precipitation. Beam broadening resulting from rain is more pronounced than that of snow and fog. Let us consider a single scattering model describing the effect of forward scattering on the attenuation, and beam broadening of a narrow laser beam. We are interested in the power distribution at the receiving plane.

Using cylindrical coordinates with origin at $T$ as illustrated in

TABLE I—FORWARD SCATTERING CORRECTION FACTOR $\bar{\beta}$ FOR A 2.6 KM PROPAGATION PATH

| Raindrop Radius (cm) | $\lambda = 0.63\mu$ $w_{oT} = 0.25$cm | $\lambda = 3.5\mu$ $w_{oT} = 0.55$cm |
|---|---|---|
| 0.025 | 0.106 | 0.025 |
| 0.050 | 0.202 | 0.049 |
| 0.075 | 0.289 | 0.071 |
| 0.100 | 0.366 | 0.093 |
| 0.125 | 0.434 | 0.113 |
| 0.150 | 0.495 | 0.133 |
| 0.175 | 0.548 | 0.152 |
| 0.200 | 0.595 | 0.169 |
| 0.225 | 0.636 | 0.186 |
| 0.250 | 0.672 | 0.202 |
| 0.275 | 0.703 | 0.217 |
| 0.300 | 0.730 | 0.232 |

$w_{oT}$ is the beam radius at which the field amplitude has fallen to $1/e$ of its maximum value in the collimated transmitting aperture.

Figure 9, the intersection of $TP$ with the receiving plane is $(\rho L/Z, \phi, L)$ whereas an arbitrary point in the receiving plane is designated by $(r, \phi', L)$. The Cartesian coordinates of these two points in the receiving plane are $(\rho L/Z \cos \phi, \rho L/Z \sin \phi, L)$ and $(r \cos \phi', r \sin \phi', L)$ respectively. Since $\theta$ is always very small for narrow laser beams, the scattering pattern of a raindrop will show negligible obliquity at the receiving plane and may be written as

$$S = \frac{2}{\pi w_s^2} \exp\left\{-\frac{2}{w_s^2}\left[\left(\frac{\rho L}{Z}\cos\phi - r\cos\phi'\right)^2 + \left(\frac{\rho L}{Z}\sin\phi - r\sin\phi'\right)^2\right]\right\} = \frac{2}{\pi w_s^2}\exp\left\{-2\left[\frac{\left(\frac{\rho L}{Z}\right)^2 + r^2}{w_s^2} + \frac{2\frac{\rho L}{Z} r\cos(\phi - \phi')}{w_s^2}\right]\right\}. \tag{15}$$

Then the scattering by a uniform rain of constant drop radius $a$ over a path of length $L$ is:

$$P_s = \int_0^L \alpha \frac{Q_{scn}}{Q_{ext}} dZ\left[\frac{1}{\frac{2}{\pi w_T^2}}\int_0^{2\pi}\int_0^\infty \frac{2}{\pi w^2} e^{-2\rho^2/w^2} S\rho\, d\rho\, d\phi\right]. \tag{16}$$

The definitions of the parameters in equations 15 and 16 are the same as in the preceding section. The integration over $\phi$ is recognized as a Bessel function of imaginary argument

$$\int_0^{2\pi} \exp\left[\frac{4\frac{\rho L}{Z} r\cos(\phi - \phi')}{w_s^2}\right] d\phi = 2\pi J_0\left(-i\frac{4\rho L r}{Z w_s^2}\right). \tag{17}$$

Using the well known identity

$$\int_0^\infty J_0(at)\exp(-p^2t^2) t\, dt = \frac{1}{2p^2}\exp\left(-\frac{a^2}{4p^2}\right) \tag{18}$$

where $a$ is an arbitrary complex number, one can perform the $\rho$-integration in equation 16:

$$2\pi\int_0^\infty J_0\left(-i\frac{4\rho L r}{Z w_s^2}\right)\exp\left[-2\rho^2\left(\frac{1}{w^2} + \frac{L^2}{Z^2 w_s^2}\right)\right]\rho\, d\rho = \frac{\pi}{2}\left(\frac{w^2 Z^2 w_s^2}{Z^2 w_s^2 + w^2 L^2}\right)\exp\left[\frac{1}{8}\left(\frac{4Lr}{Z w_s^2}\right)^2\left(\frac{w^2 Z^2 w_s^2}{Z^2 w_s^2 + w^2 L^2}\right)\right]. \tag{19}$$

Finally the $Z$-integration can be reduced to the following form for numerical computation:

$$P_s = \alpha \frac{Q_{scn}}{Q_{ext}} \int_0^L \frac{w_T^2}{w_s^2 + \left(\frac{L}{Z}\right) w^2} \exp\left[ - \frac{2r^2}{w_s^2 + \left(\frac{L}{Z}\right)^2 w^2} \right] dZ. \qquad (20)$$

Both $\alpha$ and $w_s$ in the above equation are functions of raindrop radius. Upon numerical integration of $P_s$ over the raindrop size distribution one obtains the scattering pattern in the receiving plane.

Using $L = 2.6$ km, $\lambda = 0.63\mu$, $w_{oT} = 0.25$ cm (equivalent to our experimental clear weather half-power beamwidth of twenty seconds) and the Laws-Parsons distribution, scattering patterns for a light rain 2.5 mm per hour and a heavy rain 50 mm per hour have been computed; these are shown in Figures 10(a) and 10(b), respectively. The direct beam pattern, the total power pattern, and the normalized total power pattern are also shown there. It has been tacitly assumed in the computations that the scattering and the direct beam are attenuated by the same factor, $e^{-\alpha L}$, and that the total power pattern is the arithmetic sum of the direct beam and the scattering. For light rain, (Figure 10a), the scattering modifies only

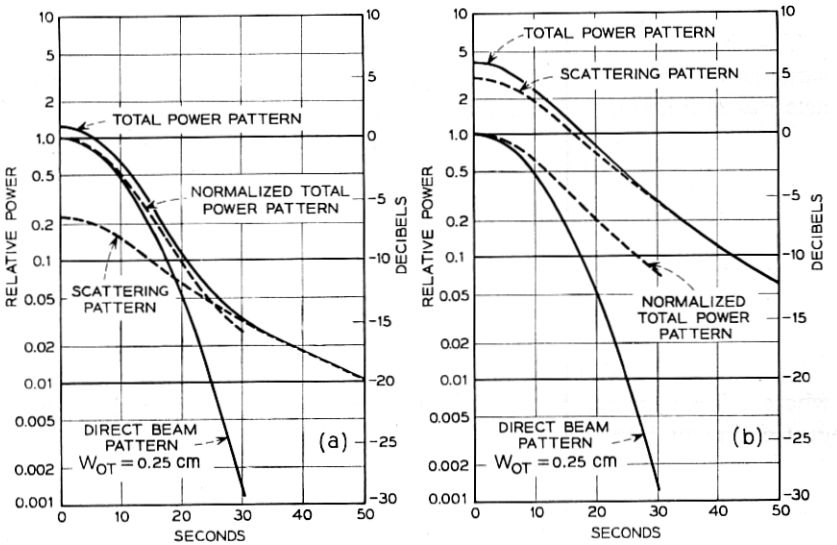


Fig. 10 — Calculated scattering pattern and beam broadening. (a) Light rain, 2.5 mm per hour. (b) Heavy rain, 50 mm per hour.

slightly the clear weather or "direct" pattern. However, in heavy rain, (Figure 10b), the scattering becomes predominant.

One might expect more beam broadening the heavier the rain; however, since the average drop size increases with rain rate, the scattering pattern of a heavy rain is narrower than that of a light rain. This effect tends to offset somewhat the beam broadening by heavy rain. On the other hand, side lobes of rain drop scattering which have been neglected in the Gaussian approximation and multiple scattering effects which are inherently absent in the single scattering model will tend to increase the beam broadening. Also notice that beam broadening will be quite sensitive to inhomogeneity of the rain.

## IV. EXPERIMENTAL EQUIPMENT

Figure 11 is a block diagram of the transmitting and receiving equipment for 0.63$\mu$ and 3.5$\mu$. Care was taken to stabilize the transmitters both thermally and mechanically. The equipment for 10.6$\mu$ has been described by Wilson and Penzias.[4] Figure 12 gives the profile of the 2.6 km propagation path at Holmdel, N. J. Table II lists the parameters of the transmitting and receiving systems.

### 4.1 *0.63$\mu$ Equipment*

The 0.63$\mu$ transmitter is a 50 mW multimode He-Ne laser; the cavity consists of two 10m-radius of curvature multilayer dielectric mirrors separated by 1.25m. The output is chopped mechanically at 330 cycles per second and passed through a refracting telescope which has an input lens of 5 cm focal length and an output lens of 50 cm focal length; the transmitting beam has a half power beamwidth of about 20 seconds in clear weather.

The received signal passes through attenuators, a 3Å bandwidth filter, a double-convex lens with an iris in the focal plane, and a polarizer to a photomultiplier. The receiver acceptance angle, about 10 minutes, is determined by the iris opening. Using a reference signal transmitted by telephone line, the synchronous detector gives a signal to noise ratio of 65 dB on a clear day; the limit of this sensitivity is set by the scattering of sunlight.

### 4.2 *3.5$\mu$ Equipment*

The 3.5$\mu$ transmitter is a 5 mW multimode He-Xe laser; the 1.1m-long cavity consists of a plane reflecting mirror and a calcite polarizer

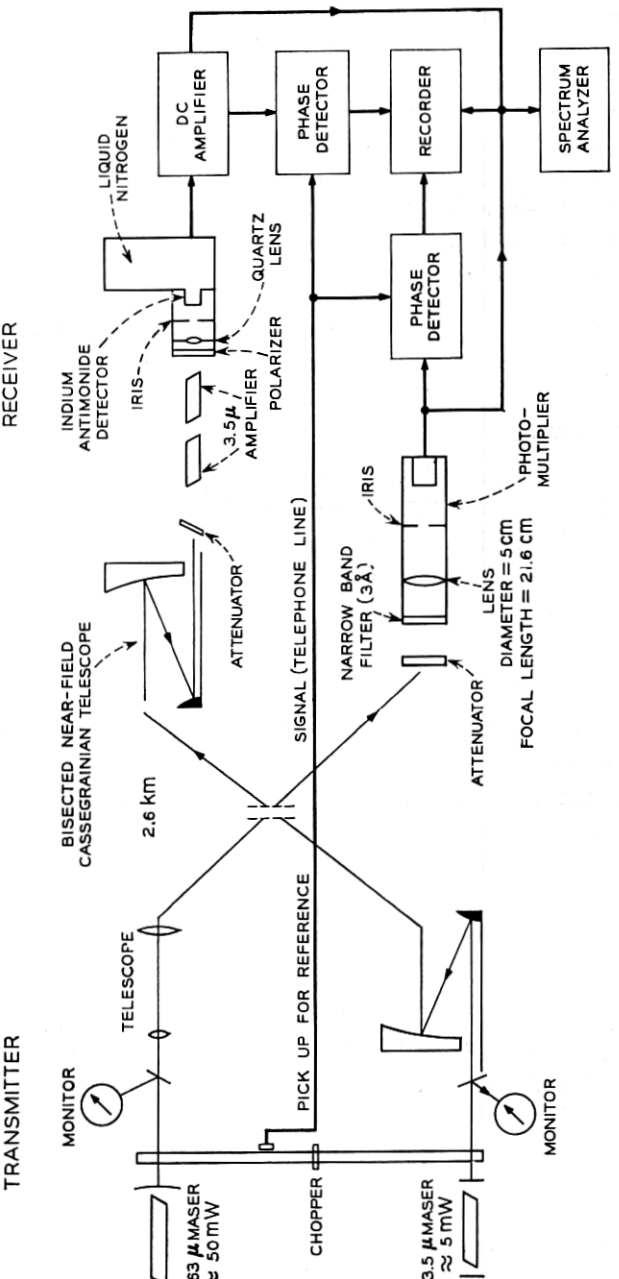


Fig. 11 — Sketch of the equipment.

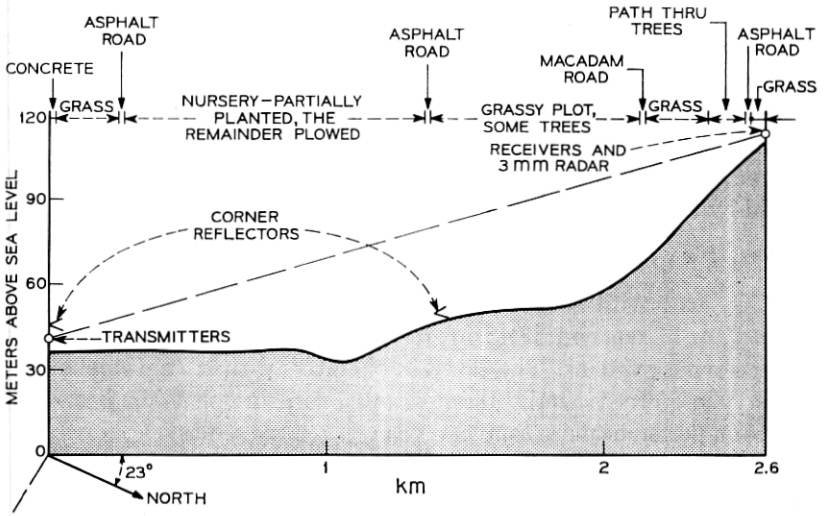


Fig. 12 — Profile of transmission path.

which acts as an output mirror. The output passes through the 330 Hz chopper to a bisected nearfield Cassegrainian telescope, a combination of two bisected confocal paraboloids. The main reflector is one half of a 38.1 cm diameter spin-cast paraboloid of 30.48 cm focal length while the subreflector has a diameter of 1.27 cm and a focal length of 1.02 cm.

Another bisected near-field telescope collects the signal for the receiver. The concentrated beam from the subreflector is amplified by two He-Xe tubes, each of about 18 dB gain. The good impedance match of the telescope plays an important role in successful application of these high-gain laser amplifiers. After the two amplifier tubes,

TABLE II — PARAMETERS OF THE TRANSMITTING AND RECEIVING SYSTEMS

| | | | |
|---|---|---|---|
| Wavelength ($\mu$) | 0.63 | 3.5 | 10.6 |
| Laser oscillator | He-Ne | He-Xe | $CO_2$ |
| Transmitter power (mW) | 50 | 5 | 500 |
| Transmitting beamwidth (rad) | $10^{-4}$ | $2 \times 10^{-4}$ | $10^{-3}$ |
| Receiving aperture diameter (cm) | 5 | 12.5 | 15 |
| Laser amplifier | None | He-Xe | None |
| Detector | Photo-multiplier | In-Sb (77°K) | Thermopile |
| Measuring range (dB) | 65 | 45 | 50 |

the signal passes through a calcite polarizer, a quartz lens, and an iris, to a liquid-nitrogen-cooled indium-antimonide photovoltaic infrared detector whose output is fed into a synchronous detection system. The receiver acceptance angle, about 1 minute of arc, is determined by the dimensions of the amplifier tubes and the telescope. A signal-to-noise ratio of 45 dB is obtained on a clear day. The receiver sensitivity is limited by the laser amplifier noise.

### 4.3 *10.6μ Equipment*

A $CO_2$ laser with an output of 0.5 W and a thermopile at the focal plane of a 15 cm collecting mirror comprise the 10.6μ transmitting and receiving systems. The laser is operated with a continuous flow of gas. Therefore, virtually uninterrupted measurement has been possible for a period of more than one year.

### 4.4 *3 mm Wavelength Radar*

The 3mm wavelength radar, based on a method used earlier for study of absorption by atmospheric gases at millimeter wavelengths,[20] provides an independent measure of the liquid water content of fogs. The system uses a klystron, modulated linearly in frequency. Two precisely constructed trihedral corner reflectors are placed on the propagation path, one near the center of the path and the other at the optical transmitter terminal (see Figure 12). Measurement of the relative power reflected from the two reflectors results in attenuation data, accurate to about 0.2 dB per km, for that portion of the path between the reflectors.

### 4.5 *Rain Gauge System*

Three gauges of the tipping-bucket type which register a pulse for each 0.25 mm of rain, are located at the transmitting site, path midpoint and the receiving site (see Figure 12). Data from the three gauges are recorded at the site of the optical receivers. No quantitative measurements are made during snow.

## V. MEASURED RESULTS

### 5.1 *Fog*

In spite of available signal-to-noise ratios of 65 dB for 0.63μ, 45 dB for 3.5μ, and 50 dB for 10.6μ, the received signal at all three wavelengths has often fallen below their noise levels during dense fog. Thus our ability to measure the wavelength dependence of attenuation by

fog is limited to relatively light fogs with attenuations less than 25 dB per km. Figure 13(a) shows that in a typical morning fog (September 21, 1965) the attenuation (in decibels) of the 3.5$\mu$ wave is about half that of the 0.63$\mu$ wave. This result may be explained by fog droplets of about 1$\mu$ diameter.

The measured data occasionally reveal a much smaller ratio as in Figure 13(b) where the 3.5$\mu$ attenuation (September 15, 1965) amounts to only one sixth of the 0.63$\mu$ attenuation; this result implies a fog with many droplets smaller than one micron.

The measured attenuation of 10.6$\mu$ in a light fog is lower than at 3.5$\mu$, as shown in Figure 13(c). At the beginning of this record (1.30 p.m. January 4, 1967), the signal at 0.63$\mu$ and 3.5$\mu$ are equal at a level of about $-15$ dB while the 10.6$\mu$ signal is at about $-2$ dB. This result can be explained, for example, by entering Figure 6(d) at a maximum drop radius of 1.3$\mu$; there, one sees that the attenuations at 0.63$\mu$ and 3.5$\mu$ are equal and exceed the 10.6$\mu$ attenuation by a factor of eight, roughly the observed value. But at 3 p.m. in Figure 13(c), the situation has changed significantly, and the ratios of the 0.63$\mu$, 3.5$\mu$, and 10.6$\mu$ attenuations are now about 15:6:1. However, if we enter Figure 6(d) at a maximum drop radius of 0.7$\mu$, the attenuation ratios are found to be very close to the observed values; thus it is found that small changes in the drop sizes can drastically affect wavelength dependence.

A percentage time distribution for the ratio of attenuation by light fog at 3.5$\mu$ and 0.63$\mu$ is plotted in Figure 14. The data, taken during seven separate fogs, were accumulated over sixteen hours during which the attenuation at either wavelength over the 2.6 km path was between 5 and 50 dB. It is seen that the median value of the ratio is 0.62 and the attenuation at 3.5$\mu$ is less than at 0.63$\mu$ 85 per cent of the time. The 15 per cent of the time that the attenuation at 3.5$\mu$ exceeds that at 0.63$\mu$ may be caused in part by equipment instability; but it can be real for certain fog parameters, such as, in Figure 6(d), $a_m = 2$ microns.

The data of Figures 4 and 6 predict that attenuation of 10.6$\mu$ is insensitive to the drop-size distribution in light fog where drop radii are about 1$\mu$. Therefore, one expects close correlation between the liquid-water density of a light fog and the measured 10.6$\mu$ attenuation.

During measurement of attenuation of the laser beams by a morning fog May 20, 1966 (Figure 15), the liquid water density of the fog was determined by measuring the attenuation of 3 mm waves. At

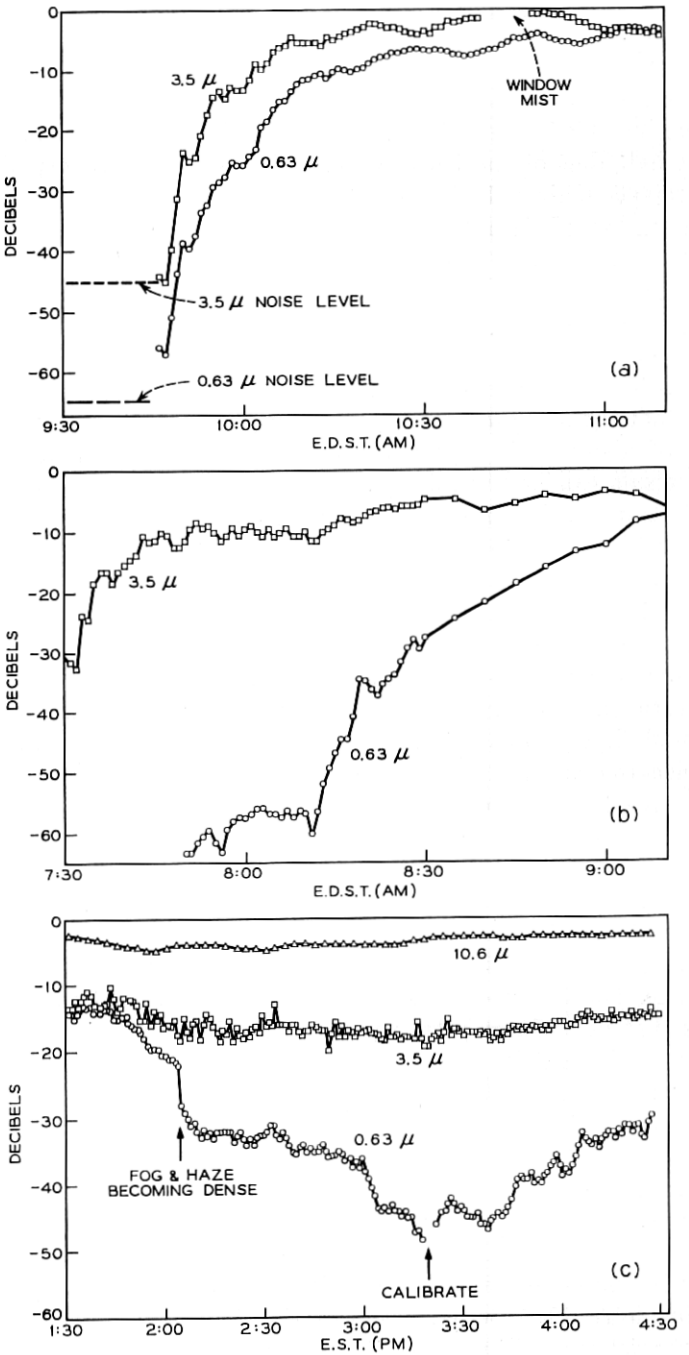


Fig. 13 — Measurement of 2.6 km transmission loss in light fog. 0 dB-signal level in clear weather.

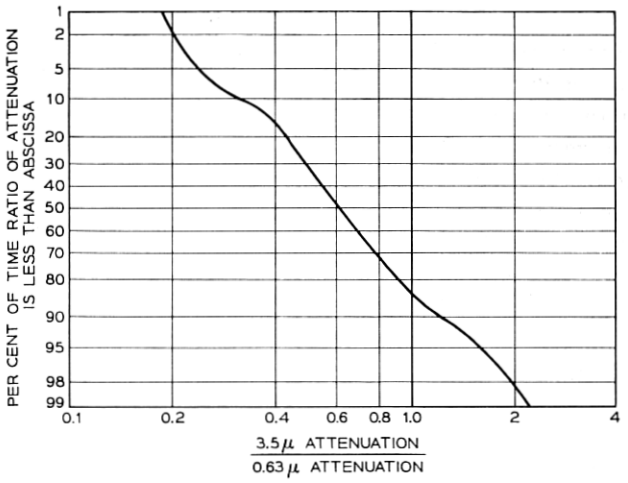


Fig. 14 — A distribution for the ratio of attenuation by light fog at 3.5$\mu$ and 0.63$\mu$.

3 mm, where the wavelength is certainly much greater than the fog-drop radius, the liquid water content is given by $M = 0.25\gamma$ gm/m$^3$, [18] $\gamma$ being the 3 mm attenuation coefficient in dB/km.

As shown in Figure 15, at 9:30 a.m. the laser beams could not be detected and the 3 mm data indicate a fog density of 0.3 gm/m$^3$. As the fog gradually lifted, the optical signals emerge in sequence above

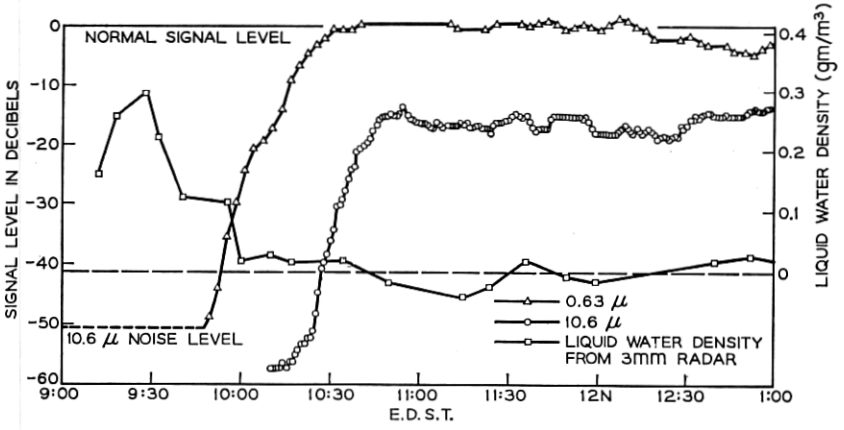


Fig. 15 — Correlation between attenuation of laser beams and liquid water content measured by a 3 mm wavelength radar in fog.

the noise level but because dense haze lingered throughout the day, the 0.63$\mu$ wave remained below the clear weather level. There is good correlation between the attenuation of the laser beams and the liquid water content of the fog obtained by the 3 mm wavelength measurement. The zero reference of the liquid water density is taken at the vanishing of the attenuation of the 10.6$\mu$ laser beam. However, precise agreement between the measured attenuation of 10.6$\mu$ and that calculated from the liquid water content obtained at 3 mm is difficult to establish because of the very small attenuation at 3 mm for light fogs. It should also be kept in mind that the fog density measured by the 3 mm radar is an average over only about half of the propagation path (see Figure 12).

### 5.2 *Rain*

Transmission through some light rains is difficult to interpret because the rain is mixed with fog; however, summer showers are very suitable for evaluating attenuation by rain. Figure 16 shows typical measured data during a summer shower; attenuation of 3.5$\mu$ is consistently about 20 per cent greater than that of 0.63$\mu$. The attenuation is well correlated with the rain rate averaged over the path. The average path rain rate is taken to be the arithmetic average of the readings of the three rain gauges described in Section 4.5, with that of the midpoint gauge carrying a double weight.

Owing to the variation in raindrop terminal velocity and drop size distribution, the relationship between the attenuation coefficient and the rain rate can be hardly expected to be linear. However, the predicted attenuation coefficient for the rain rate between 12.5 and 100 mm per hour is almost linear as shown in Figure 8. Therefore, it is justifiable to determine a least square line for measured data of attenuation by rain above a rate of 12.5 mm per hour. Figure 17 shows a least square line

$$\alpha\left(\frac{\text{dB}}{\text{km}}\right) = 0.155p\left(\frac{mm}{\text{hr}}\right) + 2.66$$

for the measured 0.63$\mu$ data of Figure 16 and two other showers.

The calculated curves for 0.63$\mu$ attenuation by rain with and without forward scattering correction (from Figure 8) have been included in Figure 17 for comparison. The good agreement between the measured line and the curve calculated with forward scattering may appear somewhat fortuitous in view of the rms deviation 2.8 dB/km. How-

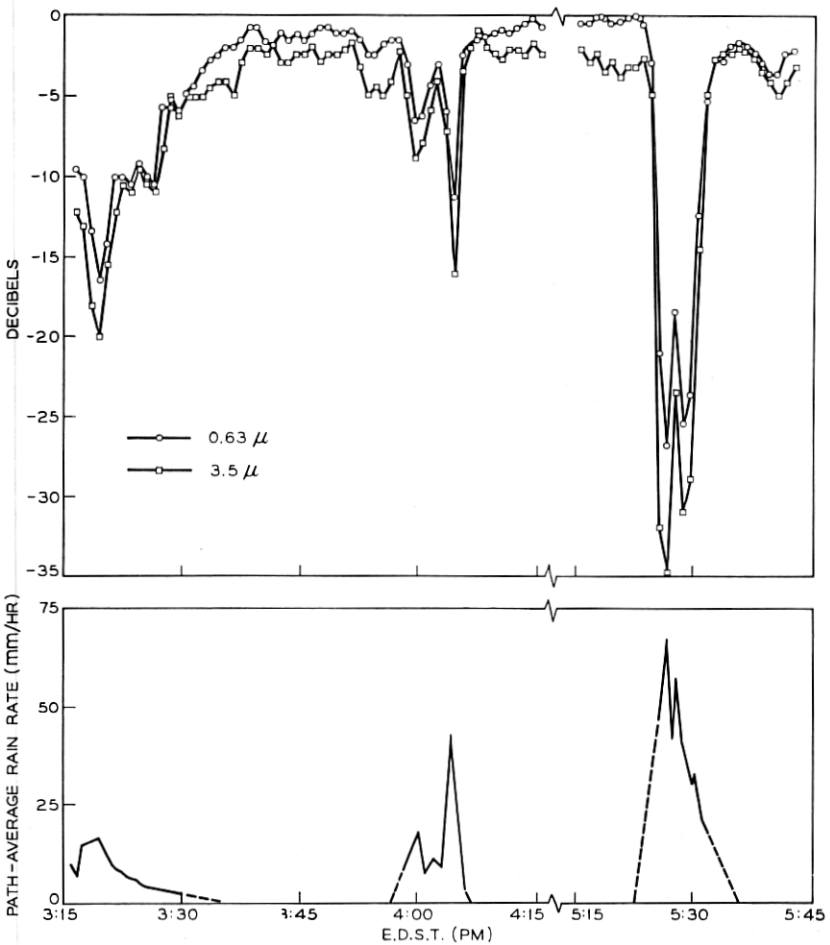


Fig. 16 — Measurement of 2.6 km transmission loss in rain showers on September 24, 1965. 0 dB-signal level in clear weather.

ever, only peak attenuations of summer showers which are relatively free of foggy conditions have been taken as measured data in Figure 17.

The relatively large rms deviation is explained as follows: the sampling of a spatially nonuniform shower by three rain gauges does not provide a satisfactory average rain rate over the 2.6 km path; the attenuation depends upon drop size distribution which may vary from one shower to another; since optical attenuation by fog is orders of

magnitude higher than that by rain, any slight mist or haze within the rain can appreciably change the measured values.

Simultaneous measurements at all three wavelengths were carried out in an unusually heavy rainstorm of September 21, 1966, during which more than 125 mm of rain accumulated. A sample of the measured data from this storm is given in Figure 18.

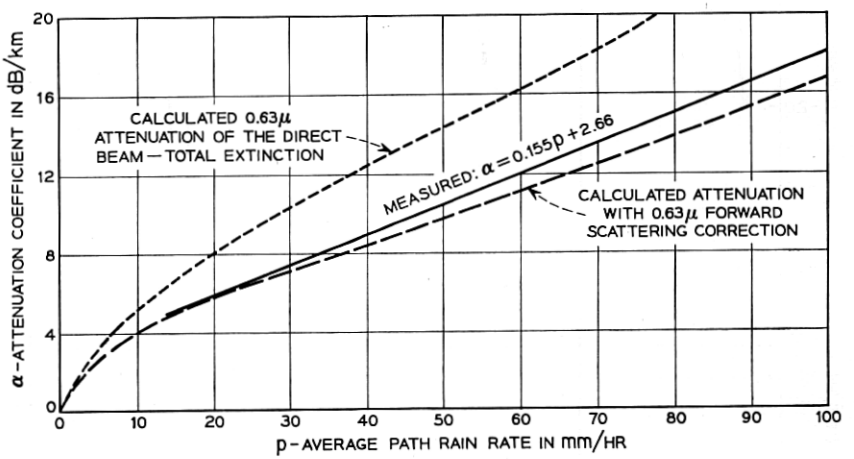


Fig. 17 — Measured rain attenuation coefficients of 0.63$\mu$ for a 2.6 km path; standard deviation is $\pm$2.8 dB per km at a rain rate of 50 mm/hr.

Points corresponding to the peak attenuations of the separate showers in the storm are plotted in Figure 19 and least-square lines for each wavelength have been drawn for rain rates between 10 and 60 mm per hour. The attenuation by rain at 10.6$\mu$ and 3.5$\mu$ is consistently greater than that at 0.63$\mu$. At 0.63$\mu$ the agreement between calculated and measured values is again rather good. Notice that the measured points at 95 mm per hour fall below the predicted curve.* When we compare Figure 19 with Figure 13(c), say, it is obvious that the wavelength dependence in propagation through rain is inverse to that through fog.

* The 0.63$\mu$ data in Figures 18 and 19 were not taken with the same receiving telescope as those of Figure 16 (5 cm diameter, see Table 1). Rather, a near-field cassegrain telescope with a collecting aperture of 600 cm was used. This change was made to determine whether or not a large receiving aperture would intercept more of the energy forward scattered by the rain (see Figures 10 and 21a) and thereby further decrease the attenuation. However, the attenuations (relative to the clear-day value) measured with the large aperture did not turn out to be significantly less than those measured with the small one.

Another sample of measured data is shown in Figure 20;† it is of particular interest because the attenuation at 0.63$\mu$ is much lower (about 18 dB) than in previous measurements and calculation for the same rain rates. The attenuation at 3.5$\mu$ and 10.6$\mu$ is only slightly below the prediction. Examination of the raw data shows that the rain distribution along the path was characterized by higher rates

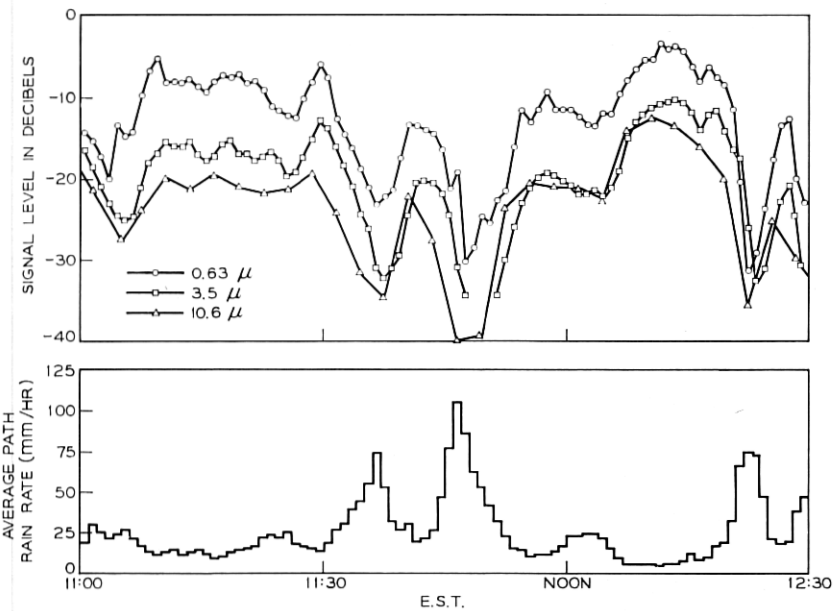


Fig. 18 — Measurement of 2.6 km transmission loss in a rain storm. 0 dB-signal level in clear weather.

near the receiving site. This observation suggests that this very low attenuation at 0.63$\mu$ is caused by a strong forward scattering contribution which is most effective when the scattering particles are near the receiver. This result is also confirmed by the measured data of the rain showers in Figure 16. There the relatively low 0.63$\mu$ attenuation coefficient measured in the second shower is also associated with a rain distribution with high concentration near the receiving site.

† The data in Figure 20 were taken with a 0.63$\mu$ transmitter beamwidth of $5 \times 10^{-4}$ radians.

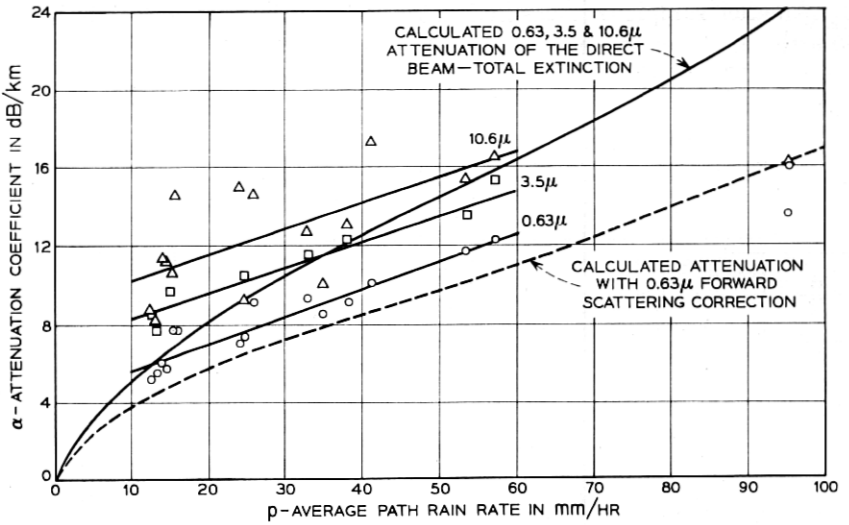


Fig. 19 — Measured attenuation coefficients of a rain storm for a 2.6 km path.

### 5.3 *Snow*

Figure 21 shows measurements of transmission loss through a light snow shower. The accumulation never exceeded about 12.5 mm per hour. Snows heavier than this have caused the signals at all three wavelengths to fall below the noise levels. The 10.6$\mu$ wave often appears to suffer greater attenuation in snow as illustrated in Figure 21; however, no definite wavelength dependence is consistently observed.

### 5.4 *A Cumulative Distribution of Attenuation at 10.6$\mu$*

In Section 4.3 we mentioned that the 10.6$\mu$ equipment operated continuously. Signal levels for the period June 1966 to May 1967 have therefore been analyzed and reduced to a cumulative distribution of attenuation as shown by the central curve in Figure 22. For example, one sees that attenuation on the 2.6 km path, resulting from all causes, exceeded 30 dB (11.5 dB/km) three per cent of the time. Also shown in the figure are distributions for the months with the highest (March) and lowest (July) outage times. Clearly, during July, a system operating at 10.6$\mu$ would be quite reliable; however, during March, heavy attenuations, mainly caused by fog, occur all too often on a 2.6 km path.

### 5.5 *Beam Broadening at 0.63μ*

Typical measured results on the beam broadening effects of rain, snow, and fog are presented in Figures 23, 24, and 25, respectively. Curve 1 in each figure is a typical clear-weather beam (about 20-second half-power beamwidth); this broadening is essentially determined by the inhomogeneities of the refractive index in the atmosphere. Notice that the clear weather beam itself is subject to modest variation but this variation is generally much less than the beam broadening observed under conditions of precipitation. The beam

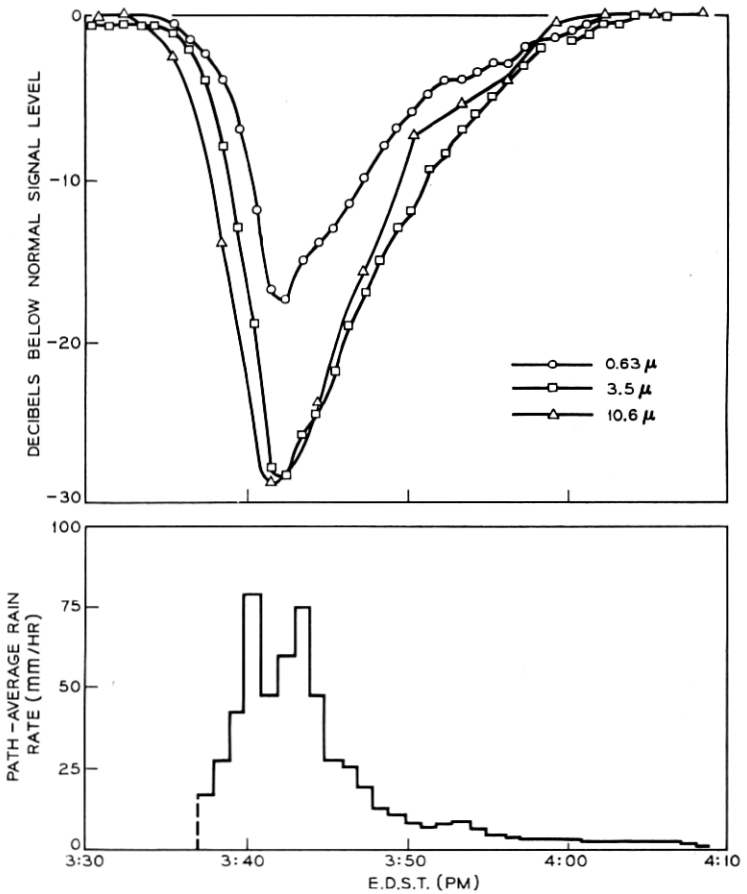


Fig. 20 — Measured attenuation over 2.6 km during a rain shower on July 11, 1967. 0 dB-signal level in clear weather.

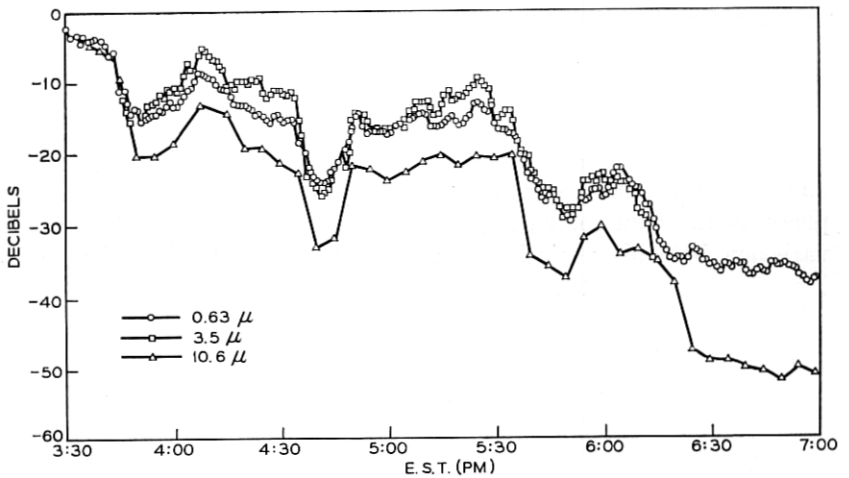


Fig. 21 — Measurement of 2.6 km transmission loss during a light snow shower on January 26, 1966. 0 dB-signal level in clear weather.

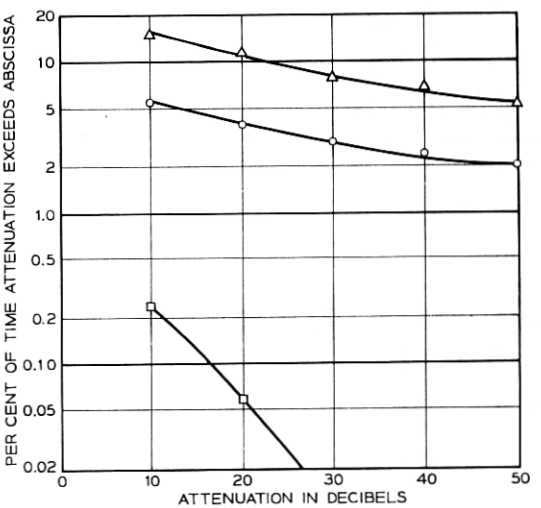


Fig. 22 — A cumulative distribution of attenuation at 10.6μ over a 2.6 km path. ○ = Average attenuation from June 1966 to May 1967. △ = March 1967, highest month. □ = July 1966, lowest month.

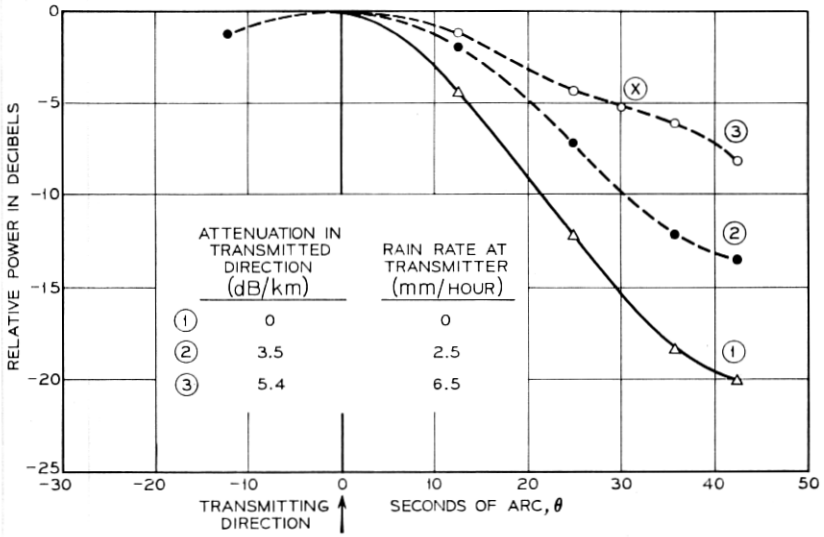


Fig. 23 — Beam broadening caused by rain.

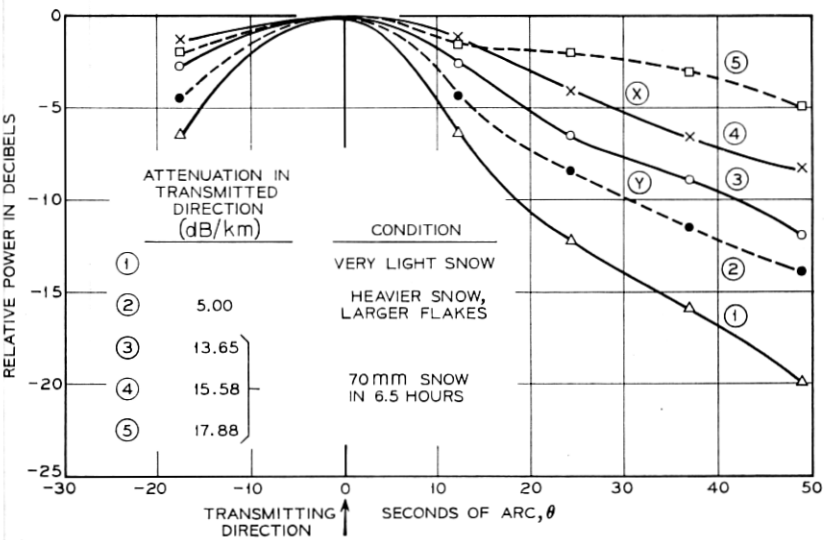


Fig. 24 — Beam broadening caused by snow.

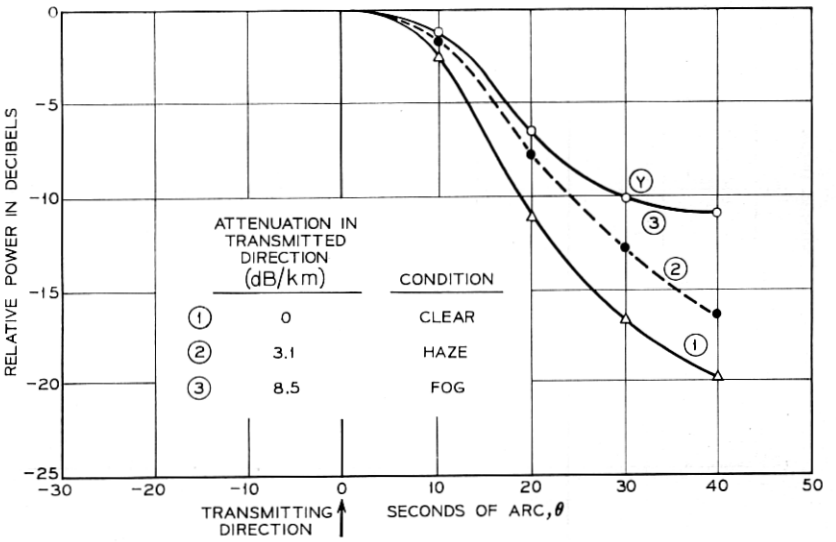


Fig. 25 — Beam broadening caused by fog.

broadening is measured by moving the receiver on a horizontal track transverse to the axis of the incident beam.

The other measured curves show beam broadening resulting from precipitation and the corresponding attenuations along with descriptions of precipitation; the curves are normalized at $\theta = 0$, the direction of the beam axis. In general, the highest attenuations correspond to the greatest beam broadening. In Figure 24, we see that the onset of beam broadening caused by snow occurs when the attenuation is fairly high. Broadening effects in the case of rain are observable at much lower attenuations (Figure 23). This is because raindrops produce more forward scattering than snow flakes which suffer from poor geometry and random orientations. Thus, the X points show the same amount of beam broadening in Figures 23 and 24; but the corresponding attenuations are 5.4 dB/km for the rain and 15.6 db/km for the snow.

Although the beam broadening, caused by fog also is readily measurable, the fog drop, being comparable in size with wavelength, is even less efficient in forward scattering than the snow flake. The Y points in Figures 24 and 25 show that the attenuation by fog is about twice that of snow for the same degree of beam broadening.

The measured beam broadening due to rain exceeds the prediction

of a single-scattering gaussian model as discussed in Section 3.2. Quantitative correlations are difficult because of the time variability and inhomogeneity of rainfall along the path.

## VI. DISCUSSIONS

A simple picture of the vast difference in attenuation of micron waves by fog and rain has been substantiated by theory and experiment. The relatively low attenuation by rain is, in part, the result of forward scattering. Owing to the difficulty of obtaining independent physical data on snow, quantitative correlation between physical measurements of precipitation and transmission has been made only for rain and fog. The predictability of attenuation of optical waves by rain is comparable to that for microwaves.[21] Indeed, visible wavelengths are attenuated less than millimeter wavelengths.

Attenuation by dense fogs often exceeds 20 dB/km. The wavelength dependence of attenuation by light fog, that is, progressively less attenuation with increasing wavelength, has been observed as expected, but the dependence is a strong function of the drop-size distribution. Similar results for incoherent light have been reported in the literature.[15, 22] Although the predicted wavelength dependence for heavy fogs which consist of drops with average radius of $5\mu$, is weaker than for light fogs, the attenuation at $10.6\mu$ would still be significantly less than at visible and shorter infrared wavelengths (see Figure 4). However, a typical dense fog of 0.1 g/m$^3$ liquid water density is calculated to attenuate $10.6\mu$ by at least 40 dB/km. Attenuation by fog at $10.6\mu$ is characterized by strong absorption and relative insensitivity to drop-size distribution.

The measured attenuation by rain, about 0.2 (dB/km)/(mm/hr) at $0.63\mu$, is consistently less (about 20 to 40 per cent) than at $3.5\mu$ and $10.6\mu$. Rain drops, which are absorbing spheres at $3.5\mu$ and $10.6\mu$, offer less scattering than at visible wavelengths and also have a less directional scattering pattern owing to the longer wavelengths.

The scattering patterns of fog drops have little directivity compared with the laser beams themselves therefore the forward scattering correction for the fog attenuation of narrow laser beams is small. If the beamwidth of the incident laser beam is comparable with the width of the scattering patterns of precipitation particles, the forward scattering will reduce the scattering loss significantly which, indeed, is mentioned in Section 5.2 for the propagation of $0.63\mu$ through

rain. Naturally the absorptive loss is not subject to any reduction. But the scattering loss of a laser beam propagating through fog cannot increase indefinitely as the fog density increases.* In particular, for a visible source radiating into a homogeneously distributed dense fog, the energy must ultimately diffuse outward in all directions, thus the free space loss of an isotropic point source appears to be the limit of the scattering loss.

When the scattering by precipitation particles is added to the attenuated original beam, a broadened beam is observed at the receiving plane; this has been illustrated by a single scattering gaussian model in Section 3.2 and by measured results in Section 5.5.

The apparent attenuation on the beam axis is reduced by the scattered component. For heavy rain, the received signal is dominated by the scattering as illustrated in Figure 10(b) and the reduction in attenuation becomes significant. When the scattering correction is small, estimates by the single scattering model (Section 3.2) and the multiple scattering model (Section 3.1) are practically the same. For relatively large corrections the multiple scattering model is expected to give a better estimate.

The precise prediction of attenuation of laser beams by precipitation in the atmosphere is hampered by the uncertainty of particle size distributions. A better knowledge of the drop size distribution is certainly desirable to provide a firm ground for the prediction of attenuation, but even a measured drop-size distribution might lead to ambiguous interpretation when the variability and inhomogeneity of the natural fog or rain is unaccounted for. Summations over unreliable drop size distributions introduce complicated-looking problems but provide little more information than a simple relation such as equation (10).

Although it is convenient to distinguish between rain and fog by a classification of drop size, one should be aware of the frequent occurrence of the intermediate states in the form of a drizzle or a mixture of rain and fog. The attenuation under these conditions has been observed to exhibit transition characteristics; however, little can be said beyond this trivial observation.

The prediction of attenuation by snow has not been touched upon here, but the experimental data indicate that it lies intermediate be-

---

* A common experience is to observe a heavy fog during daylight hours; although the sun is completely obliterated, the observer still has considerable scattered light in his environs.

tween that of rain and fog for a given amount of equivalent liquid water.

In order to evaluate relative merits of systems using different wavelengths, it is interesting to compare the attenuation by precipitation at optical wavelengths with that in other parts of the electromagnetic spectrum. Figure 26 presents the approximate attenuation coefficients for a typical dense fog and a representative shower in the frequency range from $10^{10}$ to $10^{15}$ cps.[18, 21] The absorption for a water layer containing the same amount of liquid water as the rain is also shown in Figure 26 for reference. The attenuation by rain decreases slowly from millimeter to visible wavelengths. However, the attenuation by fog is about two orders of magnitude less than that of rain at upper microwave frequencies, while the optical attenuation by fog is about two orders of magnitude greater than that of rain. Notice that, even

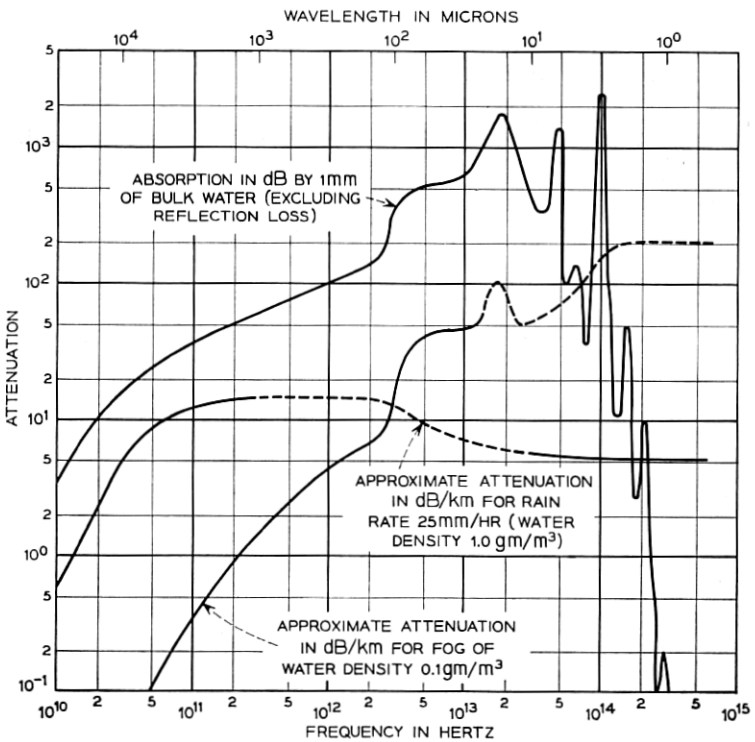


Fig. 26 — Attenuation due to liquid water in various forms as function of frequency.

at 10$\mu$, where attenuation by fog passes through a weak minimum (see Figure 26), the attenuation is still rather large as far as a practical communication system is concerned.

ACKNOWLEDGMENT

The authors are indebted to R. W. Wilson, A. A. Penzias, and A. W. Norris for the experimental data at 10.6$\mu$ and the distribution in Figure 22. Technical assistance was given by R. A. Desmond and C. A. Davison and R. A. Semplak; the computations were made by Mrs. E. Kerschbaumer.

REFERENCES

1. Chu, T. S. and Hogg, D. C., "The Attenuation of 3.392$\mu$ He-Ne Laser Radiation by Methane in the Atmosphere," B.S.T.J., *45* (February 1966), pp. 301–306.
2. Middleton, W. E. K., *Vision Through the Atmosphere,* University of Toronto Press, (1952) p. 43.
3. Hogg, D. C., "Scattering and Attenuation Due to Snow at Optical Wavelengths," Nature, *203* (July 25, 1964), p. 396.
4. Wilson, R. W. and Penzias, A. A., "Effect of Precipitation on Transmission Through the Atmosphere," Nature, *211* (September 3, 1966), p. 1081.
5. H. C., Van de Hulst, *Light Scattering by Small Particles,* New York: John Wiley and Sons (1957), chapter 11.
6. Centeno, M., "The Refractive Index of Liquid Water in the Near Infrared Spectrum," J. Opt. Soc. Amer., *31* (March 1941), pp. 244–247.
7. Bayly, J. G. and others "The Absorption Spectra of Liquid Phase $H_2O$, HDO, and $D_2O$ from 0.7$\mu$m to 10$\mu$m," Infrared Phys., *3* (December 1963), pp. 211–223.
8. Kislovskii, L. D., "Optical Characteristics of Water and Ice in the Infrared and Radio Wave Regions of the Spectrum," Opt. Spectroscopy, *7* (September 1959), pp. 201–206.
9. Curcio, J. A. and Petty, C. C., "The Near Infrared Aborption Spectrum of Liquid Water," J. Opt. Soc. Amer., *41* (May 1951), pp. 302–304.
10. Draegert, D. A., and others, "Far-Infrared Spectrum of Liquid Water," J. Opt. Soc. Amer., *56* (January 1966), pp. 64–69.
11. Eldridge, R. G., "A Few Fog Drop-Size Distributions," J. Meteorology, *18* (October 1961), pp. 671–676.
12. Diermendjian, D., "Scattering and Polarization Properties of Polydispersed Suspensions With Partial Absorption," *Electromagnetic Scattering* (Proc. Interdisciplinary Conf. Electromagnetic Scattering), ed. M. Kerker, New York: Pergamon Press, pp. 171–189, 1963.
13. Erkovich, S. P., and others, "Influence of Fog on the Range of Ground Communication Using an Optical Carrier," Tele-communications and Radio Eng., (December 1965), pp. 12–16. trans. from Russian.
14. Junge, C., "The Size Distribution and Aging of Natural Aerosols as Determined From Electrical and Optical Data on the Atmosphere," J. Meteorology, *12* (February 1955), pp. 13–25.
15. Kurnick, S. W., Zitter, R. N., and Williams, D. B. "Attenuation of Infrared Radiation by Fog," J. Opt. Soc. Amer., *50* (June 1960), pp. 578–583.
16. Saunders, M. J., unpublished work.
17. Laws, J. O. and Parsons, D. A., "The Relation of Rain Drop Size to Intensity," Trans. Amer. Geophys. Union, *24* (1943), pp. 452–460.

18. Kerr, D. E., Propagation of Short Radio Wave, New York: McGraw-Hill Book Co., Inc., 1951, Chapter 8.
19. Chu, T. S., "An Approximate Generalization of the Friis Transmission Formula," Proc. IEEE, *53* (March 1965), pp. 296–297.
20. Crawford, A. B. and Hogg, D. C., "Measurement of Atmospheric Attenuation at Millimeter Wavelengths," B.S.T.J., *35* (July 1956), pp. 907–916.
21. Medhurst, R. G., "Rainfall Attenuation of Centimeter Waves: Comparison of Theory and Measurement," IEEE Trans. Antennas and Propagation, *AP-13* (July 1965), pp. 550–564.
22. Arnulf, A., and others, "Transmission by Haze and Fog in the Spectral Region 0.35 to 10 Microns," J. Opt. Soc. Amer., *47* (June 1957), pp. 491–498.